

# High temperature ferromagnetism in Co-implanted TiO<sub>2</sub> rutile

Numan Akdogan<sup>1, ‡</sup>, Alexei Nefedov<sup>2</sup>, Hartmut Zabel<sup>3</sup>,  
Kurt Westerholt<sup>3</sup>, Hans-Werner Becker<sup>4</sup>, Christoph  
Somsen<sup>5</sup>, Şafak Gök<sup>6</sup>, Asif Bashir<sup>7</sup>, Rustam Khaibullin<sup>8,9</sup>  
and Lenar Tagirov<sup>8,9</sup>

<sup>1</sup> Department of Physics, Gebze Institute of Technology, 41400 Kocaeli, Turkey

<sup>2</sup> Lehrstuhl für Physikalische Chemie I, Ruhr-Universität Bochum, D-44780 Bochum, Germany

<sup>3</sup> Institut für Experimentalphysik/Festkörperphysik, Ruhr-Universität Bochum, D-44780 Bochum, Germany

<sup>4</sup> Institut für Physik mit Ionenstrahlen, Ruhr-Universität Bochum, D-44780 Bochum, Germany

<sup>5</sup> Institut für Werkstoffe, Ruhr-Universität Bochum, D-44780 Bochum, Germany

<sup>6</sup> Lehrstuhl für Angewandte Festkörperphysik, Ruhr-Universität Bochum, D-44780 Bochum, Germany

<sup>7</sup> Lehrstuhl für Physikalische Chemie I, Ruhr-Universität Bochum, D-44780 Bochum, Germany

<sup>8</sup> Kazan Physical-Technical Institute of RAS, 420029 Kazan, Russia

<sup>9</sup> Kazan State University, 420008 Kazan, Russia

E-mail: numan.akdogan@ruhr-uni-bochum.de

**Abstract.** We report on structural, magnetic and electronic properties of Co-implanted TiO<sub>2</sub> rutile single crystals for different implantation doses. Strong ferromagnetism at room temperature and above is observed in TiO<sub>2</sub> rutile plates after cobalt ion implantation, with magnetic parameters depending on the cobalt implantation dose. While the structural data indicate the presence of metallic cobalt clusters, the multiplet structure of the Co  $L_3$  edge in the XAS spectra gives clear evidence for a substitutional Co<sup>2+</sup> state. The detailed analysis of the structural and magnetic properties indicates that there are two magnetic phases in Co-implanted TiO<sub>2</sub> plates. One is a ferromagnetic phase due to the formation of long range ferromagnetic ordering between implanted magnetic cobalt ions in the rutile phase, and the second one is a superparamagnetic phase originates from the formation of metallic cobalt clusters in the implanted region. Using x-ray resonant magnetic scattering, the element specific magnetization of cobalt, oxygen and titanium in Co-implanted TiO<sub>2</sub> single crystals are investigated. Magnetic dichroism was observed at the Co  $L_{2,3}$  edges as well as at the O  $K$  edge. The interaction mechanism, which leads to ferromagnetic ordering of substituted cobalt ions in the host matrix, is also discussed.

PACS numbers: 85.75.-d, 78.70.Dm, 75.50.Pp, 61.72.U-

Submitted to: *J. Phys. D: Appl. Phys.*

‡ Author to whom correspondence should be addressed.

## 1. Introduction

Oxide-based diluted magnetic semiconductors (DMSs) have recently attracted considerable attention because of reports on the room temperature ferromagnetism (FM) in several systems and their projected potential for spintronic devices [1, 2]. Since Matsumoto *et al.* [3] observed room temperature FM in Co-doped anatase TiO<sub>2</sub>, much interest has been focused on the titanium dioxide as a host material for magnetic doping. Co-doped TiO<sub>2</sub> has been grown by using a wide variety of growth methods, including pulsed laser deposition (PLD) [4–7], laser molecular beam epitaxy (LMBE) [8–10], combinatorial LMBE [3, 11], reactive co-sputtering [12, 13], magnetron sputtering [14, 15], metal organic chemical-vapor deposition (MOCVD) [16], oxygen plasma assisted molecular beam epitaxy (OPA-MBE) [17–19] and as well as the sol-gel method [20]. Both the epitaxial TiO<sub>2</sub> anatase thin film and the single-crystalline TiO<sub>2</sub> rutile have also been doped by using ion implantation technique [21–27]. In addition to different growth techniques, different substrates such as Al<sub>2</sub>O<sub>3</sub> [28, 29], SrTiO<sub>3</sub> [4–6, 15, 17–19], LaAlO<sub>3</sub> [3, 5, 6, 8, 18], Si [12] and SiO<sub>2</sub>/Si [16] have been used to synthesize Co-doped TiO<sub>2</sub> films.

Many groups have observed room temperature ferromagnetism in Co-doped TiO<sub>2</sub> for both anatase and rutile phases [2, 3, 6, 12, 13, 22–25, 27, 30, 31]. A Curie temperature of about 650 K [6] and 700 K [22] was reported by different groups. Subsequent reports have concentrated on the origin of ferromagnetism in this material. Spectroscopic studies indicated that cobalt ions in thin TiO<sub>2</sub> films exist in a +2 formal oxidation state, consistent with ferromagnetism originating from Co substitution on the Ti site [4]. In other publications it is suggested that the ferromagnetic behavior is due to cobalt clustering depending on the growth conditions [3, 8, 18]. Chambers *et al.* [17] reported that the solution of Co in TiO<sub>2</sub> is possible at least up to 10% when the TiO<sub>2</sub> is deposited on SrTiO<sub>3</sub> substrate. However, when the TiO<sub>2</sub> films grown on LaAlO<sub>3</sub> substrate the solid solution is about 2-7% [3, 6]. Co metal clusters were observed in the as-grown Co-doped TiO<sub>2</sub> films with a cobalt concentration of 2%. Post-annealing of the samples leads to dissolving of clusters in the TiO<sub>2</sub> matrix [6]. For higher cobalt concentrations, bigger cobalt cluster were reported with a cluster size of about 150 nm [16].

If the observed ferromagnetism is actually due to substituted magnetic elements in the host matrix, then another important question arises; what is the coupling mechanism which leads to ferromagnetism? Recently, we have reported the observation of room temperature FM and in-plane magnetic anisotropy of single-crystalline TiO<sub>2</sub> rutile structures after high dose Co implantation [23, 24, 27]. From the observation of the in-plane magnetic anisotropy we concluded that FM in this system results from the incorporation of Co ions in the TiO<sub>2</sub> lattice, but a co-existence with Co nanoclusters could not be excluded.

In order to clarify this situation we studied the structural, magnetic and electronic properties of Co-doped (100)-oriented rutile TiO<sub>2</sub> single crystals for different implantation doses. The resulting Co:TiO<sub>2</sub> samples have been characterized by Rutherford backscattering spectroscopy (RBS) to obtain the Co depth distribution profiles and by atomic force microscopy (AFM) to check the surface properties after implantation, as well as by x-ray diffraction (XRD) and by high resolution transmission electron microscopy (TEM) to reveal the presence of precipitates and metallic Co clusters. X-ray absorption spectroscopy (XAS) has also been employed to determine whether the implanted cobalt ions are in the Co<sup>2+</sup> oxidation state or are in the

metallic state. The magnetic properties of TiO<sub>2</sub> rutile samples have been investigated using magneto-optical Kerr effect (MOKE), superconducting quantum interference device (SQUID) based magnetometry, and x-ray resonant magnetic scattering (XRMS) techniques. In addition, Hall effect measurements were carried out to verify the occurrence of intrinsic ferromagnetism and relate it to the carrier type in the samples.

## 2. Sample Preparation

40 keV Co<sup>+</sup> ions were implanted into (100)-oriented  $15 \times 15 \times 1$  mm<sup>3</sup> single-crystalline TiO<sub>2</sub> rutile substrates (from Moscow Power Engineering Institute in Russia) by using the ILU-3 ion accelerator (Kazan Physical-Technical Institute of the Russian Academy of Science) with an ion current density of  $8 \mu A \cdot cm^{-2}$ . The implantation dose varied in the range of  $0.25 - 1.50 \times 10^{17} ions \cdot cm^{-2}$ . The sample holder was cooled by flowing water during the implantation to prevent the samples from overheating. The implanted plates were cut by a diamond cutter into smaller pieces for structural, magnetic and electronic studies. As a last step, four gold contacts were evaporated on the corners of the samples for Hall effect measurements. The list of the Co-implanted TiO<sub>2</sub> samples used in the present study is given in Table 1.

**Table 1.** TiO<sub>2</sub> samples implanted with 40 keV Co<sup>+</sup> for different Co ion doses.

Sample	Dose ( $\times 10^{17} ion \cdot cm^{-2}$ )
1	0.25
2	0.50
3	0.75
4	1.00
5	1.25
6	1.50

## 3. Experimental Results

### 3.1. Structural Properties

In this section, the structural properties of non-implanted and Co-implanted TiO<sub>2</sub> rutile plates are presented. The depth distribution of implanted cobalt ions in the rutile samples as well as the cobalt concentration for each dose are determined by using the RBS technique. The RBS measurements were carried out at the Dynamic Tandem Laboratory (DTL) at the Ruhr-Universität Bochum. Fig. 1 presents the depth dependence of the cobalt concentration in Co-implanted TiO<sub>2</sub> plates for different Co ion implantation doses. The RBS data show a maximum cobalt concentration of about 25 at. % for the highest Co dose and it decreases to about 5 at. % for the lowest dose. Due to the ion sputtering of the surface during implantation, the maximum slightly shifts to the left for higher dose levels. An extended inward tail up to 70 nm due to cobalt diffusion into the volume of the rutile single crystals is also observed for each implantation dose.

Fig. 2 shows small-angle x-ray reflectivity taken with synchrotron radiation at the "Hamburg Synchrotron Radiation Laboratory" (HASYLAB) with an energy of E=8048 eV. The solid line in Fig. 2 is a fit to the data points for sample 6 ( $1.50 \times 10^{17} ions \cdot cm^{-2}$ ) from Table 2 as is obtained by the commercial software WinGIXA, which is based on the Parratt formalism [32]. Since the cobalt concentration in the

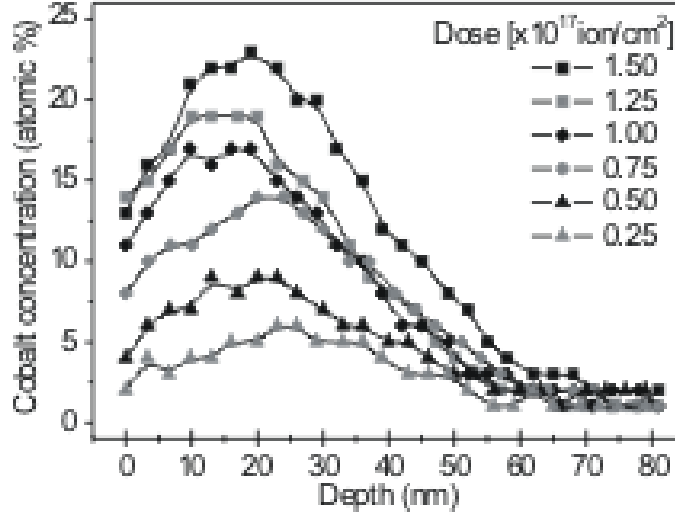


**Figure 1.** The cobalt concentration profile as a function of depth and for different implantation doses measured by RBS.

TiO<sub>2</sub> crystals changes with the depth, for fitting of the reflectivity data the implanted area is sliced into five layers. The roughness and electron density values obtained from the fit are listed in Table 2 for each layer. The model used for fitting perfectly matches the RBS data and Fig. 3 shows the depth dependence of the cobalt concentration and the normalized electron density ( $\rho_e/\rho_e(\text{TiO}_2)$ ) obtained from the fit of reflectivity. The solid line in Fig. 3 presents the calculated profile using the SRIM (*Stopping and Range of Ions in Matter*) software [33], without taking ion sputtering effects into account.

**Table 2.** Fitting parameters of reflectivity curve for sample 6 ( $1.50 \times 10^{17} \text{ ions} \cdot \text{cm}^{-2}$ ).

Layer	Thickness (nm)	Roughness ( Å )	$\rho_e (g \cdot \text{cm}^{-3})$
1. layer	11.2	26.87	4.229
2. layer	11.1	0.50	4.234
3. layer	12.1	0.71	4.227
4. layer	14.2	0.09	4.200
5. layer	20.3	9.49	4.180
Pure TiO <sub>2</sub>	—	0.09	4.170

The high angle XRD measurements were also carried out at HASYLAB, in order to detect possible impurity phases in the samples after implantation. The Bragg scans before and after implantation with different doses are shown in Fig. 4 for (100)-oriented TiO<sub>2</sub> rutile samples. Increase of the implantation dose up to  $1.50 \times 10^{17} \text{ ions} \cdot \text{cm}^{-2}$  results in two additional peaks which correspond to the (10 $\bar{1}$ 0) and (0002) reflections of hcp Co. Below the implantation dose of  $1.25 \times 10^{17} \text{ ions} \cdot \text{cm}^{-2}$  cobalt nanoclusters cannot be detected by x-ray diffraction. For every implanted sample a tail, indicated by an arrow in Fig. 4, is present around the main peak of the TiO<sub>2</sub> (200) reflection. This tail results from the expansion of the TiO<sub>2</sub> lattice upon cobalt implantation and

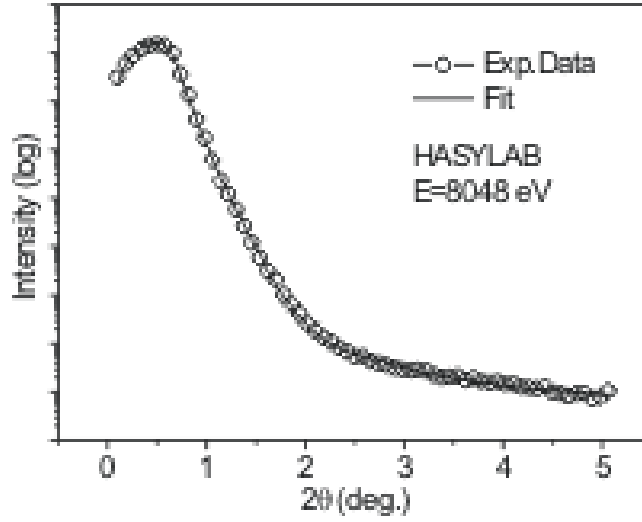


**Figure 2.** Small angle x-ray reflectivity data and fit for sample 6 ( $1.50 \times 10^{17} \text{ ions} \cdot \text{cm}^{-2}$ ).

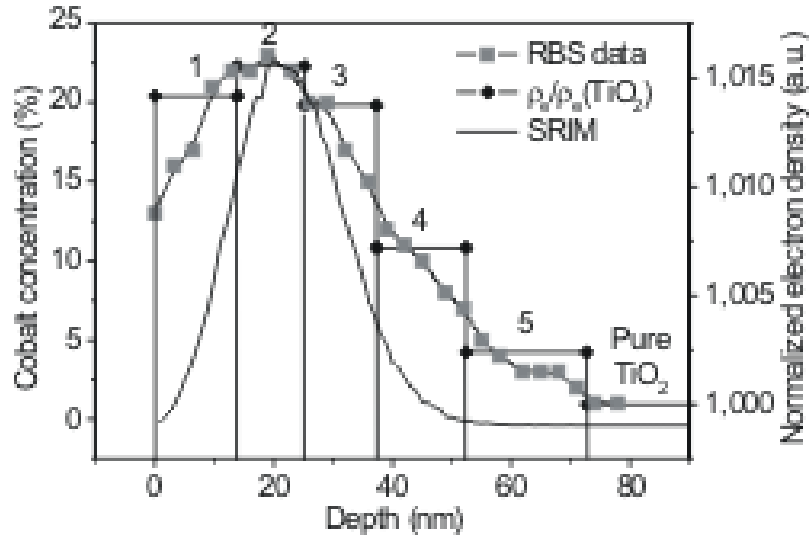


**Figure 3.** The cobalt concentration (RBS data) and the electron density determined from the small angle x-ray reflectivity as a function of depth for sample 6 ( $1.50 \times 10^{17} \text{ ions} \cdot \text{cm}^{-2}$ ). The solid line represents the calculated SRIM profile.

is not observed before the implantation. In addition, a new peak is present on the low angle side which corresponds to the spinel cobalt oxide ( $\text{Co}_3\text{O}_4$ ) phase reported already

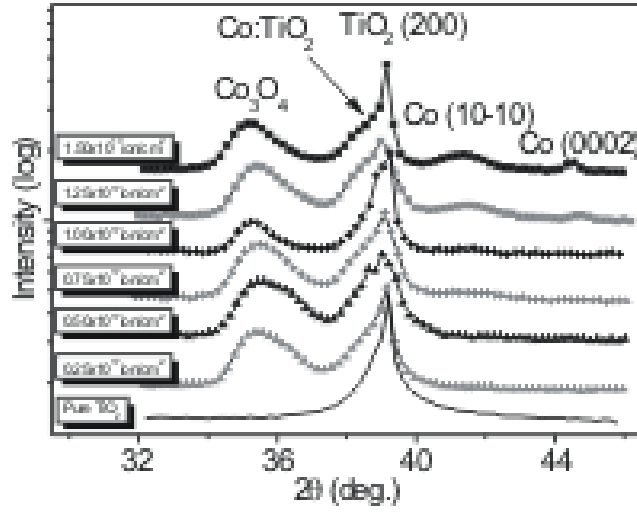


**Figure 4.** High-angle Bragg scattering scan for non-implanted (solid line) and different dose implanted (100)- $\text{TiO}_2$  samples. The presence of Co clusters is clearly seen for the highest dose (Sample 6).

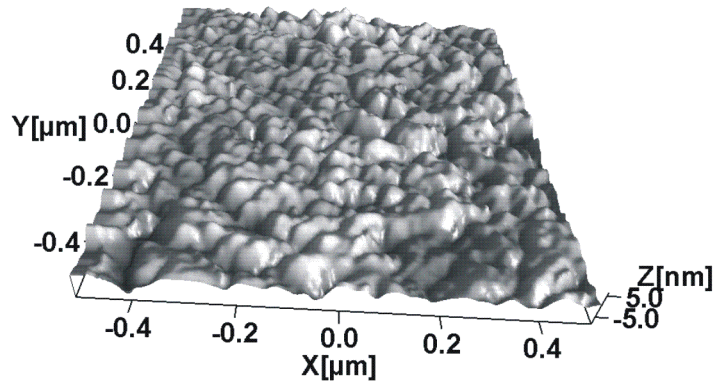


**Figure 5.** AFM surface topography of (100)- $\text{TiO}_2$  rutile after Co ion implantation with a dose of  $1.25 \times 10^{17} \text{ ions} \cdot \text{cm}^{-2}$  (Sample 5).

by Khaibullin *et al.* in Co-implanted  $\text{TiO}_2$  [31]. Due to the difference in etching rates of Co and the  $\text{TiO}_2$  during high dose ion implantation [31], cobalt nanoparticles

form on the surface and become oxidized forming antiferromagnetic Co<sub>3</sub>O<sub>4</sub> with a Neel temperature of about 40 K. Fig. 5 presents the surface morphology of sample 5 ( $1.25 \times 10^{17} \text{ ions} \cdot \text{cm}^{-2}$ ) probed by AFM (Digital Instruments NanoScope MultiMode AFM). The AFM image clearly shows a network of cobalt oxide islands on the surface with a roughness of about  $2.14 \pm 0.25 \text{ nm}$ .

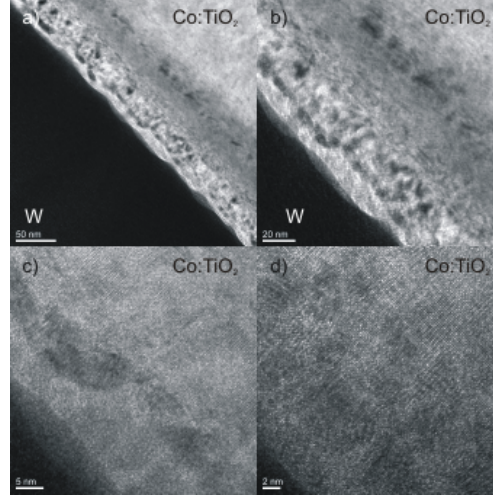


**Figure 6.** Cross-sectional TEM images of sample 6 ( $1.50 \times 10^{17} \text{ ions} \cdot \text{cm}^{-2}$ ).

For further investigations on the effects of ion implantation into TiO<sub>2</sub>, high resolution cross sectional TEM measurements were performed. For the preparation of TEM samples, the plates were thinned by focused ion beam (FIB) technique. First, the sample surface is covered by a tungsten (W) film to prevent charging effects. Then a very small cross sectional piece of the implanted sample was cut by FIB. Fig. 6 presents TEM images of sample 6 ( $1.50 \times 10^{17} \text{ ions} \cdot \text{cm}^{-2}$ ) with an increasing resolution from 50 nm to 2 nm. In Figs. 6(a) and (b), a general overview of the sample is shown. It can clearly be seen that a surface layer of about 40 nm thickness is strongly damaged after ion bombardment. There are many defects and differently sized cobalt clusters in this region. However, in Figs. 6(c) and (d) it can be recognized that the structure of TiO<sub>2</sub> is preserved after implantation. Beneath the surface layer there is another cobalt rich layer of about 40 nm thickness. Element specific TEM measurements indicate that the cobalt concentration in this layer is much smaller than in the surface layer in agreement with the RBS and x-ray reflectivity data (Fig. 3).

### 3.2. Magnetic Properties

**3.2.1. In-plane magnetic anisotropies and hysteresis measurements** In order to investigate the in-plane magnetic anisotropy of the implanted samples we used a high-resolution MOKE setup in the longitudinal configuration with s-polarized light [34–36]. The MOKE setup allows for a rotation of the sample around its surface normal (by the angle  $\varphi$ ) in order to apply a magnetic field in various in-plane directions and thus provide information about the in-plane magnetic anisotropy. The in-plane magnetic anisotropy of the samples doped with different doses as determined by the MOKE measurements are shown in Fig. 7. For the sample with the highest dose, both,

the remanent Kerr signal normalized to the Kerr signal at saturation ( $\theta_K^{rem}/\theta_K^{sat}$ ) and coercive field ( $H_C$ ), are reduced to almost zero near the hard axis ( $\varphi = 0^\circ - 180^\circ$ ), while for the magnetic field applied along the easy axis ( $\varphi = 90^\circ - 270^\circ$ ) they are close to unity. It is evident from Fig. 7 that both  $\theta_K^{rem}/\theta_K^{sat}$  and  $H_C$  exhibit a strong two-fold symmetry for the highest dose which decreases with decreasing implantation dose.

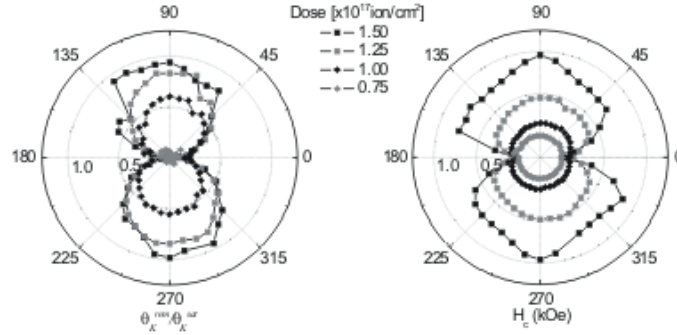


**Figure 7.** Azimuthal dependence of the normalized remanent magnetization (left) and the coercive field (right) for different Co ion doses.

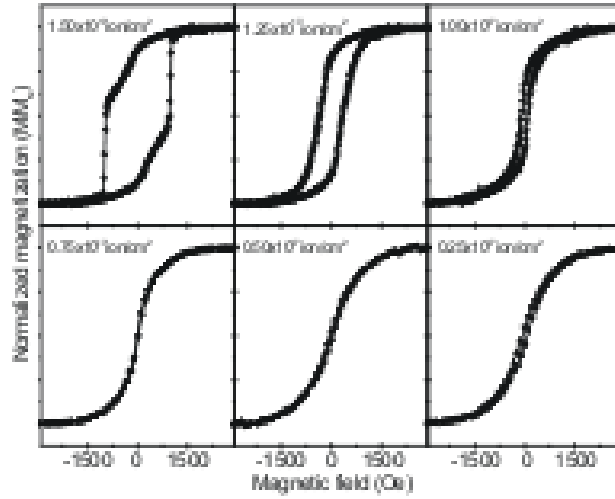


**Figure 8.** SQUID hysteresis loops for different Co ion doses taken parallel to the easy axis at T=300 K.

Hysteresis loops of the Co-implanted TiO<sub>2</sub> samples, obtained by using a Quantum Design MPMS XL SQUID magnetometer, are presented in Figs. 8 and 9. Fig. 8 shows hysteresis curves taken parallel to the easy axis at 300 K. For the highest dose ( $1.50 \times 10^{17} \text{ ions} \cdot \text{cm}^{-2}$ ) a square-like hysteresis curve is observed with a large coercive



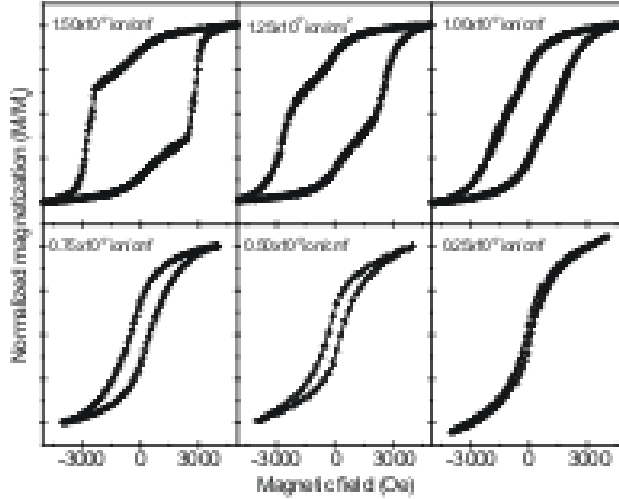


**Figure 9.** SQUID hysteresis loops for Co-implanted TiO<sub>2</sub> samples measured at 5 K along the easy axis.

field of  $H_C=950$  Oe. A rather sharp magnetization reversal takes place for this sample with a small step at 260 Oe. For the samples implanted with intermediate ion doses ( $1.00-1.25 \times 10^{17} \text{ ions} \cdot \text{cm}^{-2}$ ), the recorded  $M-H$  loops also show hysteretic behavior, but the coercive fields decrease significantly. The remanent magnetization normalized to the saturation magnetization also decreases for the intermediate doses. At 5 K the two step feature in the hysteresis curve is not only present for the highest dose but also for intermediate doses (Fig. 9). The low dose implanted samples exhibit at low temperatures a typical superparamagnetic behavior with a pronounced paramagnetic contribution to the hysteresis curves .

In order to further investigate the effect of cobalt clusters, we have performed temperature dependent magnetization ( $M-T$ ) measurements using a SQUID magnetometer. Fig. 10 presents field cooled (FC) and zero field cooled (ZFC) plots for each sample. For ZFC measurements, the samples are cooled in zero field to 5 K and the magnetization is recorded during warming up to 390 K in an applied field of 100 Oe parallel to the film surface. For FC measurements the applied field of 100 Oe is kept during cooling to 5 K and the magnetization is recorded during field warming with the same field value. The FC (black squares) and ZFC (grey circles) curves diverge substantially for all doses and the peak in the ZFC curve progressively shifts to higher temperatures with increasing cobalt concentration. This behavior is not expected for a ferromagnet and suggests the presence of magnetic cobalt nanoparticles in the films or a spin-glass like nature of the system [37, 38]. The  $M-T$  curve of sample 1 ( $0.25 \times 10^{17} \text{ ions} \cdot \text{cm}^{-2}$ ) is rather unusual and may be attributed to the coexistence of a weak ferromagnetic and a superparamagnetic phase with a transition temperature of about 30 K. The  $M-T$  curves for films with higher cobalt concentrations ( $0.50-0.75 \times 10^{17} \text{ ions} \cdot \text{cm}^{-2}$ ) indicate the occurrence of superparamagnetism with a blocking temperature of about 100 K and 250 K for sample 2 ( $0.50 \times 10^{17} \text{ ions} \cdot \text{cm}^{-2}$ )

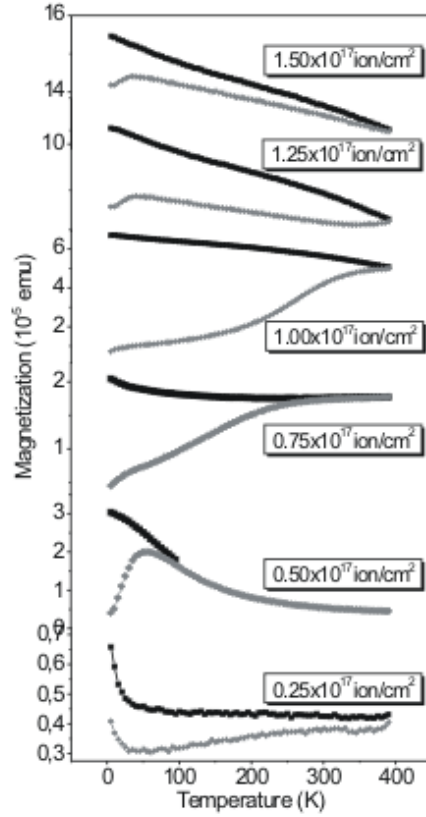


**Figure 10.** FC (black squares) and ZFC (grey circles) magnetization curves of Co-implanted TiO<sub>2</sub> rutile samples taken using a SQUID magnetometry.

and sample 3 ( $0.75 \times 10^{17} \text{ ions} \cdot \text{cm}^{-2}$ ), respectively. The temperature dependence of sample 4 is similar to that of sample 2 and sample 3 except the blocking temperature is much higher, namely above 390 K. It is also important to note that the FC curve of this sample shows a more or less continuous behavior versus temperature which is typical for ferromagnets. The reported room temperature ferromagnetism with a two fold in-plane magnetic anisotropy in this sample indicates that for this dose substituted cobalt ions start to interact ferromagnetically. The FC and ZFC curves of sample 5 ( $1.25 \times 10^{17} \text{ ions} \cdot \text{cm}^{-2}$ ) and sample 6 ( $1.50 \times 10^{17} \text{ ions} \cdot \text{cm}^{-2}$ ) are much closer to each other. This progression indicates that the ferromagnetic phase becomes dominant in these samples. The observation of a two component hysteresis at RT for sample 6 supports this argument. Small peaks in the ZFC curves at low temperatures of these samples indicate the existence of superparamagnetic cobalt clusters. These clusters are also clearly seen in the TEM images of sample 6 (Fig. 6).

**3.2.2. XRMS and XAS measurements** To shed more light on the origin of room temperature ferromagnetism in Co-doped TiO<sub>2</sub>, the magnetic properties of Co-implanted TiO<sub>2</sub> rutile films have also been investigated using the XRMS and XAS

techniques. Both the XRMS and XAS experiments were carried out at the undulator beam lines UE56/1-PGM and UE52-SGM at BESSY II (Berlin, Germany) using the ALICE diffractometer [39]. The diffractometer comprises a two circle goniometer and works in horizontal scattering geometry. A maximum magnetic field of  $\pm 2700 \text{ Oe}$  can be applied in the scattering plane along the sample surface either parallel or antiparallel to the photon helicity, which corresponds to the longitudinal magneto-optical Kerr effect (L-MOKE) geometry. The magnetic contribution to the scattered intensity (XRMS) was always measured by reversing the magnetic field direction while keeping the photon helicity fixed. Thus, by tuning the energy to the Co  $L_3$  absorption edge (780 eV), reflectivity scans were taken and the magnetic splitting for plus and minus field was clearly seen (presented in Ref. [25]). As a compromise between high scattering intensity and high magnetic sensitivity for the investigation of the magnetic properties via energy scans at the Co  $L$  edges, the scattering angle was fixed at the position of  $2\theta = 8.2^\circ$  (the angle of incidence  $\theta = 4.1^\circ$ ) [25]. For measurements at the O  $K$  edge ( $E=535 \text{ eV}$ ) the scattering angle was fixed at  $2\theta = 12^\circ$ , which corresponds to the same scattering vector in the reciprocal space.

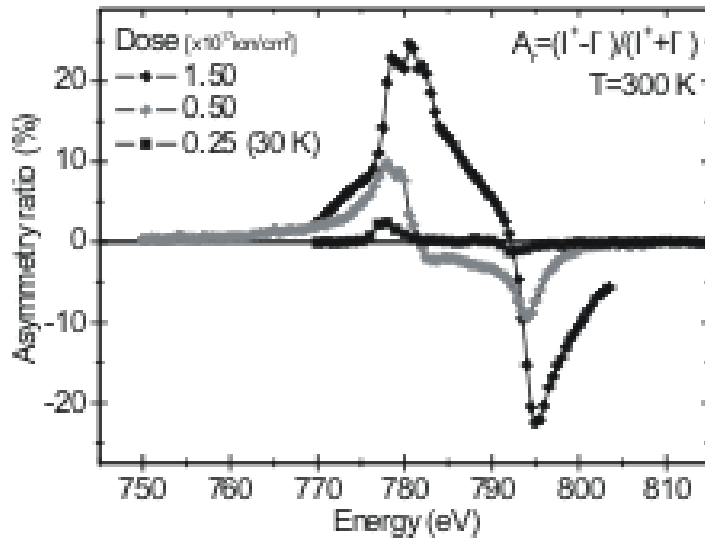


**Figure 11.** Dose dependence of the asymmetry ratio at the Co  $L_{2,3}$  edges measured at saturation field.

First, we measured the energy dependence of the scattered intensity (XRMS) around the Co  $L_{2,3}$  edges. Since the magnetic contribution to the resonant scattering can best be visualized by plotting the asymmetry ratio ( $A_r = (I^+ - I^-)/(I^+ + I^-)$ ), in Fig. 11 we present the dose dependence of the asymmetry ratio at the Co  $L$  edges measured in saturation at room temperature. Only the lowest dose of  $0.25 \times 10^{17} \text{ ions} \cdot \text{cm}^{-2}$  is measured at 30 K. The magnetization of the samples decreases by decreasing the Co ion dose in agreement with SQUID hysteresis curves and previous MOKE measurements [27]. It is important to note that the fine structure around the

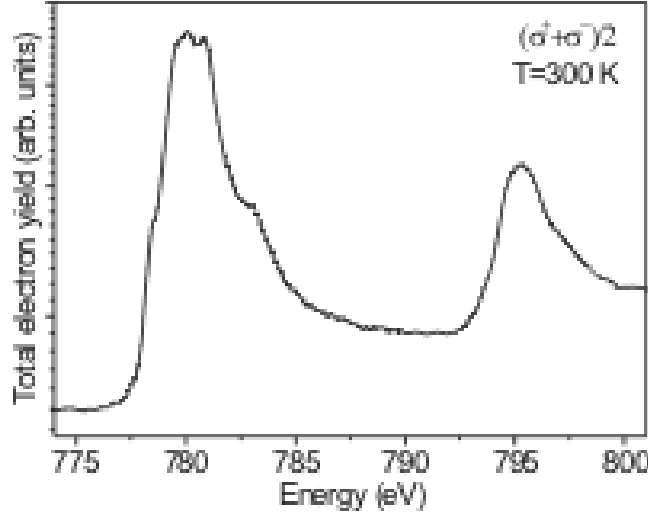


**Figure 12.** X-ray absorption spectra of sample 6 measured at the Co  $L_{2,3}$  edges, determined by total electron yield.  $\sigma^+$  and  $\sigma^-$  denote the right and left circular polarization of the incident light, respectively.

Co  $L_3$  edge, which is clearly seen in the asymmetry ratio in Fig. 11 for sample 6, is not typical for metallic cobalt. It is well known that in the case of metallic films the absorption spectra around the  $L_3$  peak of Co consists of a single component [40]. This fine structure of the Co  $L_3$  peak is similar to that observed before for CoO films [40], and it is indicative of a  $\text{Co}^{2+}$  state. To make this situation more clear and to record comparable results with previous reports [8], we performed XAS experiments. The absorption data were taken by the total electron yield (TEY) method, i.e. by measuring the sample drain current. Since the external magnetic field changes the excited electron trajectories, the XAS spectra were measured with fixed photon helicity in remanence. The angle of incidence was set again to  $4.1^\circ$  with respect to the surface. The absorption spectra were normalized to the incoming photon flux measured from the beam line mirror. The averaged x-ray absorption spectra  $(\sigma^+ + \sigma^-)/2$  at the Co  $L_{2,3}$  edges is shown in Fig. 12. The XAS spectrum clearly shows a multiplet structure at the Co  $L_3$  edge. This multiplet structure is a strong indication for the Co ions being in the  $\text{Co}^{2+}$  state in this sample.

The magnetic signal at the Ti  $L_{2,3}$  and the O  $K$  edges was also investigated for sample 6. Fig. 13 and Fig. 14 show the corresponding asymmetry ratios. Within the sensitivity limit no magnetic signal could be recorded for Ti and O at room temperature. However, at the O  $K$  edge, a small but clearly visible magnetic signal was observed at  $T=30$  K [25]. It should be mentioned that the oxygen polarization has also been observed for samples with lower dose (dose levels of  $1.00 - 1.25 \times 10^{17} \text{ ions} \cdot \text{cm}^{-2}$ ). For samples implanted with doses below  $1.00 \times 10^{17} \text{ ions} \cdot \text{cm}^{-2}$ , the magnetic signal at the O  $K$  edge is below the sensitivity limit of the experimental setup.

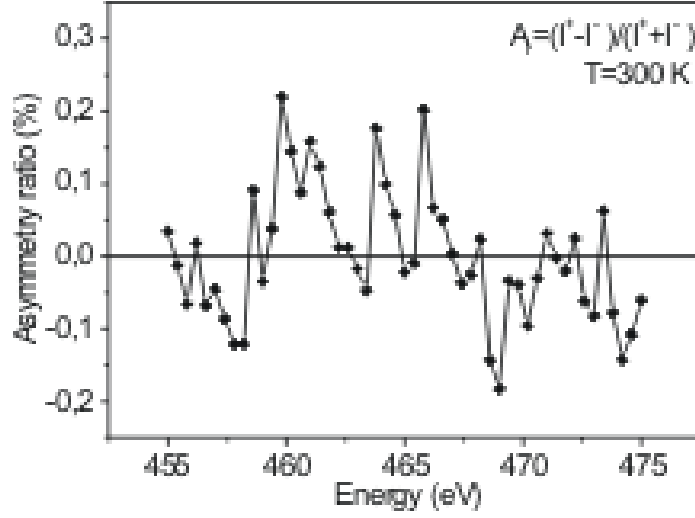


Figure 13. Asymmetry ratio measured at the Ti  $L_{2,3}$  edges for sample 6.

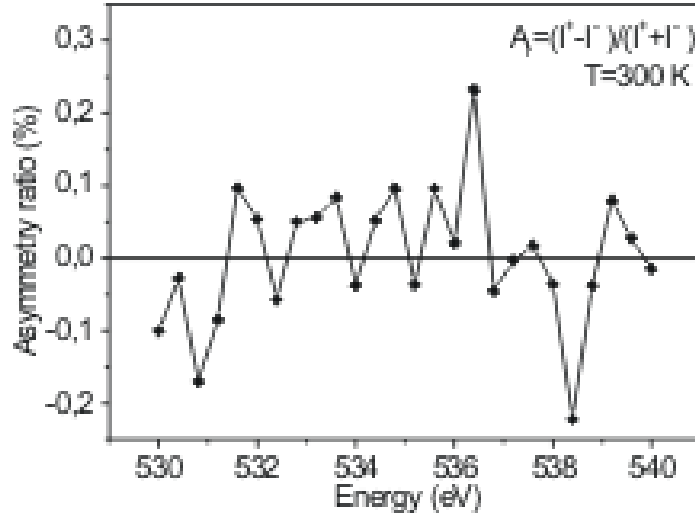
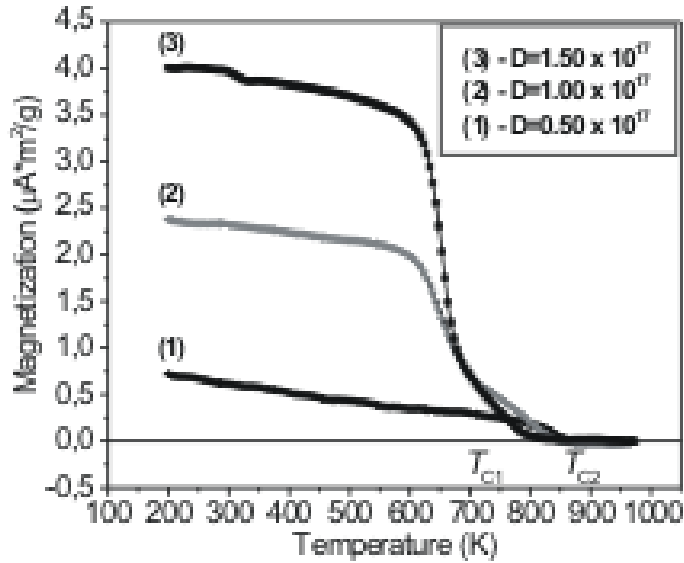


Figure 14. Asymmetry ratio taken at the O  $K$  absorption edge for sample 6.

**3.2.3. High temperature magnetization experiments** In order to determine the Curie temperatures ( $T_C$ ) of Co:TiO<sub>2</sub> samples, we have carried out thermomagnetic measurements using the Faraday balance technique [41] by heating the samples from 100 K (ZFC) up to 1000 K with a rate of 100 K/min in air and at an applied field of 2 kOe. In Fig. 15 we show the magnetization curves for

TiO<sub>2</sub> rutile plates implanted with different doses. The sample with a dose of  $0.50 \times 10^{17} \text{ ions} \cdot \text{cm}^{-2}$  shows the magnetic/non-magnetic transition temperature at about 850 K (curve 1). For the samples 4 ( $1.00 \times 10^{17} \text{ ions} \cdot \text{cm}^{-2}$ ) and 6 ( $1.50 \times 10^{17} \text{ ions} \cdot \text{cm}^{-2}$ ), two magnetic ordering temperatures of  $T_{C1} \sim 700$  K and  $T_{C2} \sim 850$  K, were observed (curves 2 and 3). This shows that two ferromagnetic phases, a “low temperature” and a high-temperature” phase, coexist in these samples. The contribution to the magnetization from the high-temperature phase decreases gradually with increasing the cobalt implantation dose. Finally, for the sample with the highest dose of  $1.50 \times 10^{17} \text{ ions} \cdot \text{cm}^{-2}$ , the low-temperature phase dominates, while the high-temperature phase practically disappears (curve 3).



**Figure 15.** High temperature magnetization curves measured in a field of 2000 Oe for TiO<sub>2</sub> rutile samples implanted by cobalt ions with different doses.

It should be stated here that the high temperature magnetization curves presented in Fig. 15 are irreversible, i.e. on cooling down the ferromagnetic signal disappears. From this we infer that some diffusion process or recrystallization may occur, which should not be confused with a real Curie temperature. Furthermore, the magnetization versus temperature does not follow the shape of a usual order parameter. On the other hand, after vacuum annealing the samples at high temperatures [31],  $T_{C1}$  reappears but not  $T_{C2}$ , indicating that  $T_{C1}$  is more intrinsic than  $T_{C2}$ . This point clearly needs some further investigations. For the present purpose, it is important to note that a stable ferromagnetic phase exists at room temperature and far beyond, which may be very useful for high temperature applications of DMSs.

#### 4. Hall effect measurements

The observation of an anomalous Hall effect (AHE) is suggested to be one of the important criteria for DMS materials to be intrinsically ferromagnetic [42, 43]. In the past, several groups reported the AHE in highly reduced TiO<sub>2</sub> films doped with either with Co or Fe, from which they infer the possibility of intrinsic ferromagnetism in these samples [7, 9, 44]. However, recently, Shinde *et al.* [45] reported the co-occurrence of superparamagnetism and AHE in highly reduced Co-doped TiO<sub>2</sub> rutile films, raising questions about the usefulness of the AHE as a test of the intrinsic nature of ferromagnetism in DMS materials without a detailed characterization of the sample.

In magnetic materials, in addition to the ordinary Hall effect (OHE), there is an additional voltage proportional to the sample magnetization [46], the so-called anomalous Hall effect. Hence, the Hall voltage can be written as follows [46],

$$V_H = \left( \frac{R_0 I}{t} \right) H \cos \alpha + \left( \frac{R_A \mu_0 I}{t} \right) M \cos \theta, \quad (1)$$

where  $t$  is the film thickness and  $I$  is the current.  $R_0$  and  $R_A$  are the ordinary and anomalous Hall effect coefficients, respectively.  $\mu_0$  is the permeability of free space.  $\alpha$  is the angle between the applied magnetic field ( $H$ ) and the film normal.  $\theta$  is the angle between the sample magnetization ( $M$ ) and the sample normal. The first term in Eq. 1 is the ordinary Hall effect and arises from the Lorentz force acting on conduction electrons. This establishes an electric field perpendicular to the applied magnetic field and to the current. The second term is the anomalous Hall effect and it is conventionally attributed to spin dependent scattering mechanism involving a spin-orbit interaction between the conduction electrons and the magnetic moments of the material. At low applied magnetic fields, the Hall voltage ( $V_H$ ) is dominated by the magnetic field dependence of the sample magnetization  $M$ . When the applied magnetic field is high enough to saturate the sample magnetization, the magnetic field dependence of the Hall voltage becomes linear due to the ordinary Hall effect.

The Hall effect measurements were carried out at 4.2 K using a van der Pauw configuration presented in Fig. 16 as an inset. In spite of the fact that the structural and the magnetization measurements indicate the presence of magnetic nanoparticles in the Co-implanted TiO<sub>2</sub> films, the anomalous Hall effect is observed for these samples. The Hall effect data of sample 6 are shown in Fig. 16. As it is explained above, a rapid increase in the Hall voltage at low fields can be interpreted as an AHE which is followed by a slow decrease corresponding to the ordinary Hall effect. It is important to note that the negative slope of the high field data indicates  $n$ -type carriers in Co-implanted TiO<sub>2</sub> rutile. The electron density ( $n$ ), calculated from the slope of the curve at higher fields, is about  $3.75 \times 10^{18} \text{ cm}^{-3}$ .

#### 5. Discussion

The origin of the observed two magnetic phases (ferromagnetism and superparamagnetism) in Co-implanted TiO<sub>2</sub> rutile plates is attributed to the formation of two cobalt enriched layers with different cobalt concentrations and valence states of the cobalt dopant. The TEM images (Fig. 6) clearly show that nanosize magnetic particles of cobalt metal nucleate in the surface region of the implanted rutile where the cobalt concentration is maximal (see RBS data in Fig. 1). Mostly beneath this layer, in the

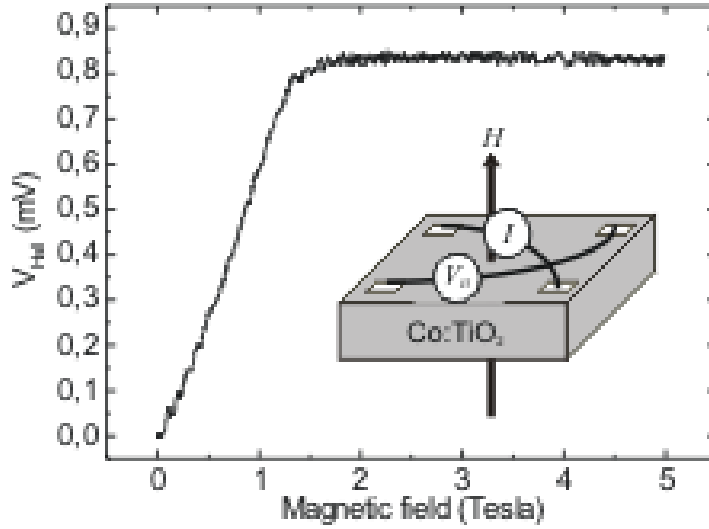


**Figure 16.** Hall effect data of sample 6 taken at 4.2 K. Inset shows the geometry of the Hall effect experiments.  $H$  is the external magnetic field applied perpendicular to the film surface.

tail of the depth profile, the implanted cobalt can exist in an ionic state substituting the  $\text{Ti}^{4+}$  ions in the matrix by  $\text{Co}^{2+}$  ions. Thus for charge neutrality either two  $\text{Co}^{2+}$  ions substitute for one  $\text{Ti}^{4+}$  ion, or one  $\text{Co}^{2+}$  ion and one oxygen vacancy are formed. At the lowest dose ( $0.25 \times 10^{17} \text{ ions} \cdot \text{cm}^{-2}$ ) the magnetic contribution from the metallic cobalt clusters and the substituted cobalt ions is very small, and hence the MOKE signal at room temperature is rather weak. Increasing the cobalt implantation dose leads to both, an increase of the Co cluster size, as seen by the increasing blocking temperature, and to more substitutional cobalt in the  $\text{Co}^{2+}$  state. At certain concentrations the substituted cobalt ions start to interact leading to ferromagnetism at room temperature in sample 4 ( $1.00 \times 10^{17} \text{ ions} \cdot \text{cm}^{-2}$ ) and sample 5 ( $1.25 \times 10^{17} \text{ ions} \cdot \text{cm}^{-2}$ ). At doses higher than  $1.25 \times 10^{17} \text{ ions} \cdot \text{cm}^{-2}$  strong ferromagnetic order is formed due to the ion accumulation and indirect exchange interaction between the  $\text{Co}^{2+}$  ions. However, TEM images, peaks in the ZFC curves, and two component hysteresis curves for dose levels  $1.25 - 1.50 \times 10^{17} \text{ ions} \cdot \text{cm}^{-2}$  indicate that the superparamagnetic phase is present in these samples and coexists with the ferromagnetic phase.

Revealing the interaction mechanism of substituted cobalt ions which leads to ferromagnetism in  $\text{Co:TiO}_2$  is also an important incentive of this study. Since the XAS spectra clearly show the multiplet structure of the Co  $L_3$  peak (see Fig. 12), it is certain that some portion of the implanted cobalt ions in  $\text{TiO}_2$  rutile are in the  $\text{Co}^{2+}$  oxidation state. When  $\text{TiO}_2$  is doped with cobalt ions, simultaneously oxygen vacancies are also expected to be produced [47]. The observation of the AHE in the Co-implanted rutile samples give clear evidence for oxygen vacancies which contribute to shallow donor states in  $\text{TiO}_2$  and increase the carrier density [48]. It was suggested



that these oxygen vacancies strongly promote ferromagnetism in Co-implanted TiO<sub>2</sub> films by an indirect exchange of substituted cobalt ions through electrons trapped by neighboring oxygen vacancies [49].

We have also noticed a clear polarization of the oxygen  $p$ -orbitals in Co-implanted TiO<sub>2</sub> rutile samples. The shape of the hysteresis curve and the coercive field measured at the O  $K$  edge is the same as the one recorded at the Co  $L_3$  edge [25]. This is a clear indication that oxygen ions, which are close to Co ions in TiO<sub>2</sub> become magnetically polarized. Whether the oxygen polarization is essential for supporting ferromagnetic exchange is presently not clear.

Another important result of this study is the observation of an anomalous Hall effect. The AHE is often taken as an evidence that the charge carriers are polarized and that the material is a true DMS. However, after simultaneous observation of superparamagnetism and AHE in Co-doped TiO<sub>2</sub> films by Shinde *et al.* [45] and also in this study, the existence of an AHE can be thought of a necessary measurement condition but it is not sufficient by itself to claim the intrinsic nature of ferromagnetism in a DMS material.

## 6. Summary and conclusions

In conclusion, we have studied in detail the structural, magnetic and electronic properties of Co-implanted TiO<sub>2</sub> rutile films for different implantation doses. The structural data clearly show that cobalt clusters are present in the samples after high dose cobalt ion implantation. In addition to the cluster formation, substitution of cobalt ions into the rutile lattice is also confirmed by XAS experiments. The origin of the observed magnetic behavior in the samples is explained by the coexistence of two different magnetic phases. Cobalt nanoparticles in the surface layer form a superparamagnetic phase in the samples implanted with low and intermediate doses. In addition, substitution of Ti<sup>4+</sup> ions by Co<sup>2+</sup> ions leads to intrinsic ferromagnetism as a second magnetic phase. The oxygen vacancies formed by ion implantation provide charge compensation and serve as mediators for the exchange interaction between the Co<sup>2+</sup> ions in high dose doped samples. The observation of the anomalous Hall effect in Co-implanted TiO<sub>2</sub> rutile can also be thought of an important indicator for the observed long range ordered intrinsic ferromagnetism in the rutile phase. At the highest dose, a strong ferromagnetic phase exists with a Curie temperature of above 700 K. This ferromagnetic phase exhibits a perfect uniaxial in-plane magnetic anisotropy following exactly the crystal symmetry of the TiO<sub>2</sub> rutile. We consider this as the strongest experimental evidence for the intrinsic nature of ferromagnetism in the Co-doped TiO<sub>2</sub> rutile.

### 6.1. Acknowledgments

We wish to acknowledge A. Kröger for preparation of TEM samples, and O. Seeck and W. Caliebe (HASYLAB) for their assistance with the beamline operation. This work was partially supported by BMBF through Contracts Nos. 05KS4PCA (ALICE Chamber) and 05ES3XBA/5 (Travel to BESSY), by DFG through SFB 491, and by RFBR through the grant Nos 07-02-00559-a and 04-02-97505-r. N. Akdoğan acknowledges a fellowship through the IMPRS-SurMat.

## References

- [1] Matsukura F, Ohno H and Dietl T 2002 *III-V Ferromagnetic Semiconductors, in Handbook of Magnetic Materials*, edited by K. H. J. Buschow (Elsevier)
- [2] Janisch R, Gopal P and Spaldin N A 2005 *J. Phys.: Condens. Matter.* **17** R657
- [3] Matsumoto Y, Murakami M, Shono T, Hasegawa T, Fukumura T, Kawasaki M, Ahmet P, Chikyow T, Koshihara S Y and Koinuma H 2001 *Science* **291** 854
- [4] Kim D H, Yang J S, Lee K W, Bu S D, Noha T W, Oh S J, Kim Y W, Chung J S, Tanaka H, Lee H Y and Kawai T 2002 *Appl. Phys. Lett.* **81** 2421
- [5] Stampe P, Kennedy R, Xin Y and Parker J 2003 *J. Appl. Phys.* **93** 7864
- [6] Shinde S R, Ogale S B, Sarma S D, Simpson J R, Drew H D, Lofland S E, Lanci C, Buban J P, Browning N D, Kulkarni V N, Higgins J, Sharma R P, Greene R L and Venkatesan T 2003 *Phys. Rev. B* **67** 115211
- [7] Higgins J S, Shinde S R, Ogale S B, Vankatesan T and Greene R L 2004 *Phys. Rev. B* **69** 073201
- [8] Kim J Y, Park J H, Park B G, Noh H J, Oh S J, Yang J S, Kim D H, Bu S D, Noh T W, Lin H J, Hsieh H H and Chen C T 2003 *Phys. Rev. Lett.* **90** 017401
- [9] Toyosaki H, Fukumura T, Yamada Y, Nakajima K, Chikyow T, Hasegawa T, Koinuma H and Kawasaki M 2004 *Nature* **3** 221
- [10] Murakami M, Matsumoto Y, Hasegawa T, Ahmet P, Nakajima K, Chikyow T, Ofuchi H, Nakai I and Koinuma H 2004 *J. Appl. Phys.* **95** 5330
- [11] Fukumura T and et al 2003 *Japan J. Appl. Phys.* **42** L105
- [12] Park W, Ortega-Hertogs R, Moodera J, Punnoose A and Seehra M 2002 *J. Appl. Phys.* **91** 8093
- [13] Rameev B Z, Yildiz F, Tagirov L R, Aktas B, Park W K and Moodera J S 2003 *J. Magn. Magn. Mater.* **258** 361
- [14] Yang H and Singh R 2004 *J. Appl. Phys.* **95** 7192
- [15] Balagurov L, Klimonsky S, Kobeleva S, Orlov A, Perov N and Yarkin D 2004 *JETP Lett.* **79** 98
- [16] Seong N J, Yoon S G and Cho C R 2002 *Appl. Phys. Lett.* **81** 4209
- [17] Chambers S A, Thevuthasan S, Farrow R F C, Marks R F, Thiele J U, Folks L, Samant M G, Kellock A J, Ruzycki N, Ederer D L and Diebold U 2001 *Appl. Phys. Lett.* **79** 3467
- [18] Chambers S A, Wang C M, Thevuthasan S, Droubay T, McCready D E, Lea A S, Shutthanandan V and Windisch C F J 2002 *Thin Solid Films* **418** 197
- [19] Chambers S A, Droubay T, Wang C M, Lea A S, Farrow R F C, Folks L, Deline V and Anders S 2003 *Appl. Phys. Lett.* **82** 1257
- [20] Soo Y L, Kioseoglou G, Kim S, Kao Y H, Devi P S, Parise J, Gambino R J and Gouma P I 2002 *Appl. Phys. Lett.* **81** 655
- [21] Kim D H, Yang J S, Kim Y S, Kim D W, Noh T W, Bu S D, Kim Y W, Park Y D, Pearton S J, Jo Y and Park J G 2003 *Appl. Phys. Lett.* **83** 4574
- [22] Khaibullin R I, Tagirov L R, Rameev B Z, Ibragimov S Z, Yildiz F and Aktas B 2004 *J. Phys.: Condens. Matter* **16** L443
- [23] Akdogan N, Rameev B Z, Dorosinsky L, Sozeri H, Khaibullin R I, Aktas B, Tagirov L R, Westphalen A and Zabel H 2005 *J. Phys.: Cond. Matter* **17** L359
- [24] Akdogan N, Rameev B Z, Khaibullin R I, Westphalen A, Tagirov L R, Aktas B and Zabel H 2006 *J. Magn. Magn. Mater.* **300** e4
- [25] Nefedov A, Akdogan N, Zabel H, Khaibullin R I and Tagirov L R 2006 *Appl. Phys. Lett.* **89** 182509
- [26] Pinto J V, Cruz M M, da Silva R C, Franco N, Casaca A, Alves E and Godinho M 2007 *The European Physical Journal B* **55** 253
- [27] Akdogan N, Nefedov A, Westphalen A, Zabel H, Khaibullin R I and Tagirov L R 2007 *Superlatt. and Microstr.* **41** 132
- [28] Matsumoto Y, Takahashi R, Murakami M, Koida T, Fan X J, Hasegawa T, Fukumura T, Kawasaki M, Koshihara S Y and Koinuma H 2001 *Japan J. Appl. Phys.* **40** L1204
- [29] Suryanarayanan R, Naik V, Kharel P, Talagala P and Naik R 2005 *Solid State Commun.* **133** 439
- [30] Prellier W, Fouchet A and Mercey B 2003 *J. Phys.: Condens. Matter.* **15** R1583
- [31] Khaibullin R I, Ibragimov S Z, Tagirov L R, Popok V N and Khaibullin I B 2007 *Nucl. Instr. and Meth. in Phys. Res. B* **257** 369
- [32] Parratt L G 1954 *Phys. Rev.* **95** 359
- [33] Ziegler J F, Biersack J P and Littmark U 1985 *The Stopping and Range of Ions in Solids* (Pergamon Press, New York)
- [34] Zeidler T, Schreiber F, Zabel H, Donner W and Metoki N 1996 *Phys. Rev. B* **53** 3256
- [35] Schmitte T, Westerholt K and Zabel H 2002 *J. Appl. Phys.* **92** 4524

- [36] Westphalen A, Lee M S, Remhof A and Zabel H 2007 *Rev. Sci. Instruments* **78** 121301
- [37] Shand P M, Christianson A D, Pekarek T M, Martinson L S, Schweitzer J W, Miotkowski I and Crooker B C 1998 *Phys. Rev. B* **58** 12876
- [38] Hocheppied J F and Pileni M P 2000 *J. Appl. Phys.* **87** 2742
- [39] Grabis J, Nefedov A and Zabel H 2003 *Rev. Sci. Instr.* **74** 4048
- [40] Regan T J, Ohldag H, Stamm C, Nolting F, Lüning J, Stöhr J and White R L 2001 *Phys. Rev. B* **64** 214422
- [41] Bourov B, Iasonov P, Nourgaliev D and Ibragimov S 1996 *Ann. Geophys.* **14** 133
- [42] Ohno H, Shen A, Matsukura F, Oiwa A, Endo A, Katsumoto S and Iye Y 1996 *Appl. Phys. Lett.* **69** 363
- [43] Matsukura F, Ohno H, Shen A and Sugawara Y 1998 *Phys. Rev. B* **57** R2037
- [44] Wang Z, Wang W and Tang J 2003 *Appl. Phys. Lett.* **83** 518
- [45] Shinde S R, Ogale S B, Higgins J S, Zheng H, Millis A J, Kulkarni V N, Ramesh R, Greene R L and Vankatesan T 2004 *Phys. Rev. Lett.* **92** 166601
- [46] Hurd C M 1972 *The Hall Effect in Metals and Alloys* (Plenum Press, New York)
- [47] Errico L A, Renteria M and Weissmann M 2005 *Phys. Rev. B* **72** 184425
- [48] Yahia J 1963 *Phys. Rev.* **130** 1711
- [49] Coey J M D, Venkatesan M and Fitzgerald C B 2005 *Nature Materials* **4** 173